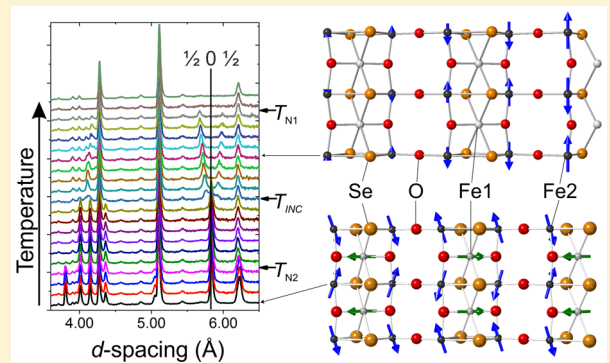


Complex Magnetic Ordering in the Oxide Selenide $\text{Sr}_2\text{Fe}_3\text{Se}_2\text{O}_3$ Simon J. Cassidy,[†] Fabio Orlandi,[‡] Pascal Manuel,[‡] Joke Hadermann,[§] Alex Scrimshire,^{||} Paul A. Bingham,^{||} and Simon J. Clarke^{*,†}[†]Department of Chemistry, University of Oxford, Inorganic Chemistry Laboratory, South Parks Road, Oxford OX1 3QR, United Kingdom[‡]ISIS Facility, STFC Rutherford Appleton Laboratory, Harwell Oxford, Didcot OX11 0QX, United Kingdom[§]Electron Microscopy for Materials Science (EMAT), University of Antwerp, Groenenborgerlaan 171, B-2020 Antwerp, Belgium^{||}Materials and Engineering Research Institute, Faculty of Arts, Computing, Engineering and Sciences, Sheffield Hallam University, City Campus, Howard Street, Sheffield S1 1WB, United Kingdom**S** Supporting Information

ABSTRACT: $\text{Sr}_2\text{Fe}_3\text{Se}_2\text{O}_3$ is a localized-moment iron oxide selenide in which two unusual coordinations for Fe^{2+} ions form two sublattices in a 2:1 ratio. In the paramagnetic region at room temperature, the compound adopts the crystal structure first reported for $\text{Sr}_2\text{Co}_3\text{S}_2\text{O}_3$, crystallizing in space group Pbam with $a = 7.8121 \text{ \AA}$, $b = 10.2375 \text{ \AA}$, $c = 3.9939 \text{ \AA}$, and $Z = 2$. The sublattice occupied by two-thirds of the iron ions (Fe2 site) is formed by a network of distorted *mer*- $[\text{FeSe}_3\text{O}_3]$ octahedra linked via shared Se_2 edges and O vertices forming layers, which connect to other layers by shared Se vertices. As shown by magnetometry, neutron powder diffraction, and Mössbauer spectroscopy measurements, these moments undergo long-range magnetic ordering below $T_{\text{N}1} = 118 \text{ K}$, initially adopting a magnetic structure with a propagation vector $(1/2 - \delta, 0, 1/2)$ ($0 \leq \delta \leq 0.1$) which is incommensurate

with the nuclear structure and described in the $\text{Pbam}1'(a01/2)000s$ magnetic superspace group, until at 92 K (T_{INC}) there is a first order lock-in transition to a structure in which these Fe2 moments form a magnetic structure with a propagation vector $(1/2, 0, 1/2)$ which may be modeled using a $2a \times b \times 2c$ expansion of the nuclear cell in space group $36.178 \text{ B}_a\text{b}_2\text{m}$ (BNS notation). Below $T_{\text{N}2} = 52 \text{ K}$ the remaining third of the Fe^{2+} moments (Fe1 site) which are in a compressed *trans*- $[\text{FeSe}_4\text{O}_2]$ octahedral environment undergo long-range ordering, as is evident from the magnetometry, the Mössbauer spectra, and the appearance of new magnetic Bragg peaks in the neutron diffractograms. The ordering of the second set of moments on the Fe1 sites results in a slight reorientation of the majority moments on the Fe2 sites. The magnetic structure at 1.5 K is described by a $2a \times 2b \times 2c$ expansion of the nuclear cell in space group $9.40 \text{ I}_a\text{b}$ (BNS notation).



INTRODUCTION

Multianion compounds adopt a diverse range of structures and have received recent attention in several contexts. Oxide sulfides and oxide selenides enable band gap tuning for semiconductors and transparent conductors^{1–3} and are of interest as potential thermoelectric materials.⁴ Superconductors based on iron arsenides⁵ and selenides⁶ also often contain oxide or hydroxide⁷ slabs separating the iron arsenide or selenide layers. In oxide chalcogenides ordering of the oxide and heavier chalcogenide (S^{2-} , Se^{2-} , or Te^{2-}) anions is the norm as a result of their differing sizes and chemistry.⁸ Layered crystal structures often result, in which cations of main group and transition metals are separated according to their oxo- and chalcophilicity. Often, transition metal cations in oxide chalcogenides have coordination environments that contain both anions, e.g., in structures such as that of $\text{La}_2\text{Fe}_2\text{Se}_2\text{O}_3$ ⁹ which has layers composed of face-sharing *trans*- $[\text{FeSe}_4\text{O}_2]$ octahedra separated by PbO -type LaO layers. Sometimes the

resulting structures are less obviously layered but maintain some low-dimensional feature of the magnetic exchange interactions which results in unusual phenomena such as in $\text{SrFe}_2\text{Se}_2\text{O}$, which contains FeSe_2O_2 tetrahedra that link to form what has been described as a spin-ladder with multiple competing exchange interactions.¹⁰ Some multianion coordination environments are inherently polarized such as those in CaFeSeO ^{11–13} and CaFeSO ¹⁴ which contain all-vertex-linked FeSe_2O_2 and S-vertex-linked FeS_3O tetrahedra, respectively, and which crystallize in different structures, both with noncentrosymmetric space groups (CaFeSeO also has a centrosymmetric polymorph).¹¹ The oxide selenide $\text{Sr}_2\text{Fe}_3\text{Se}_2\text{O}_3$ has recently been reported by Lai et al.,¹⁵ along with the sulfide analogues for both Fe¹⁵ and Co,¹⁶ in work which has been carried out independently of our own. In

Received: June 4, 2018

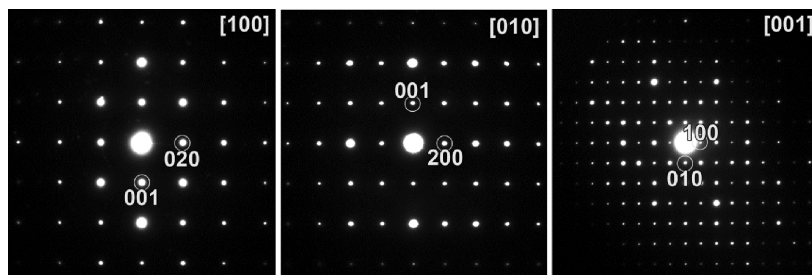


Figure 1. Electron diffractograms of $\text{Sr}_2\text{Fe}_3\text{Se}_2\text{O}_3$ along the major zone axes.

$\text{Sr}_2\text{Fe}_3\text{Se}_2\text{O}_3$ and $\text{Sr}_2\text{Fe}_3\text{S}_2\text{O}_3$ ¹⁵ a new coordination environment for Fe^{2+} is described, and there are a succession of magnetic phase transitions on cooling to a state in which all the Fe^{2+} ions are participating in magnetic long-range order. Here we use neutron powder diffraction (NPD) and Mössbauer spectroscopy to probe the magnetic ordering as a function of temperature and correlate the behavior with the detailed analysis of magnetometry and Mössbauer data made by Lai et al.¹⁵

EXPERIMENTAL SECTION

Synthesis. Polycrystalline samples of $\text{Sr}_2\text{Fe}_3\text{Se}_2\text{O}_3$ were synthesized from stoichiometric amounts of SrO , FeSe , Fe_2O_3 (Alfa Aesar 99.998%), and Fe (Alfa Aesar 99.998%). The SrO was prepared by thermal decomposition of SrCO_3 (Alfa Aesar 99.997%) under dynamic vacuum for 16 h at 800 °C followed by 4 h at 1100 °C. FeSe was prepared by stoichiometric reaction of iron (Alfa Aesar 99.998%) and selenium (Alfa Aesar 99.999%) powders at 700 °C for 48 h. The four reactants were ground together inside an argon-filled dry glovebox (Glovebox Technology Ltd, UK) using an agate pestle and mortar. The ground powder was pressed into a pellet, placed inside an alumina crucible, and sealed inside an evacuated silica ampule. Various heating protocols were then investigated as described in the results section.

Diffraction Measurements. Laboratory X-ray powder diffraction (XRPD) measurements to monitor phase purity and the course of the reactions were performed on a Panalytical Empyrean diffractometer using $\text{Cu K}\alpha_1$ radiation. High-resolution XRPD measurements for structure solution and analysis were performed on beamline I11¹⁷ at the Diamond Light Source, Ltd., United Kingdom, and additional measurements were made on beamline ID22 at the European Synchrotron Radiation Facility (ESRF), France. NPD measurements were performed from 10–300 K on the WISH instrument¹⁸ at the ISIS Pulsed Neutron and Muon Facility, United Kingdom, with the samples contained in indium-sealed thin-walled vanadium cylinders. Structure solution and Rietveld refinements were performed using the TOPAS Academic software.¹⁹ Electron diffraction measurements at EMAT, Antwerp, were acquired with a Philips CM20 transmission electron microscope operated at 200 kV with the sample prepared by grinding the crushed powder in ethanol and depositing a few drops of the suspension on holey carbon TEM grids.

Magnetometry. All measurements used a Quantum Design MPMS-XL SQUID magnetometer. The susceptibility was determined by measuring the magnetization as a function of temperature on warming from 2 to 300 K after cooling both in a zero applied field: zero-field-cooled (ZFC) and in the measuring field: field-cooled (FC) of 50 mT. Magnetization isotherms ($-5 \leq \mu_0 H/T \leq +5$) at several temperatures were each measured after cooling the sample from 200 K (i.e., well above the highest magnetic ordering transition) to the measurement temperature in a +5 T field and then measuring the magnetization while sweeping the field in steps down to -5 T and back to +5 T. Successive isotherms were collected from highest to lowest temperature. Between the measurement of successive isotherms, the field was changed to 0 T and the sample warmed to 200 K, then the field was changed to +5 T prior to cooling. This was

in an attempt to remove any influence of the previous measurement on the next. Samples were sequestered from air in gelatin capsules.

Mössbauer Spectroscopy. ^{57}Fe Mössbauer spectra were collected using a constant-acceleration, cryostatic spectrometer (Janis 10 K CCR, model CCS-800/204N) with a Lakeshore 335 temperature controller. The radiation source $^{57}\text{Co}(\text{Rh})$ was kept at room temperature. A Mössbauer thickness of 1²⁰ was achieved by homogeneously mixing 25 mg of $\text{Sr}_2\text{Fe}_3\text{Se}_2\text{O}_3$ with graphite to fully pack a cylindrical cavity (1.77 cm² cross section, 0.1 cm thick) in an acrylic disc, which was sealed airtight. Spectra were analyzed using the Recoil software package²¹ to deconvolve the data into separate iron environments. Extracted chemical shift values are quoted relative to a thin $\alpha\text{-Fe}$ foil calibration.

RESULTS AND DISCUSSION

Synthesis. A preliminary synthesis using only SrO and FeSe in equimolar quantities was found to produce the

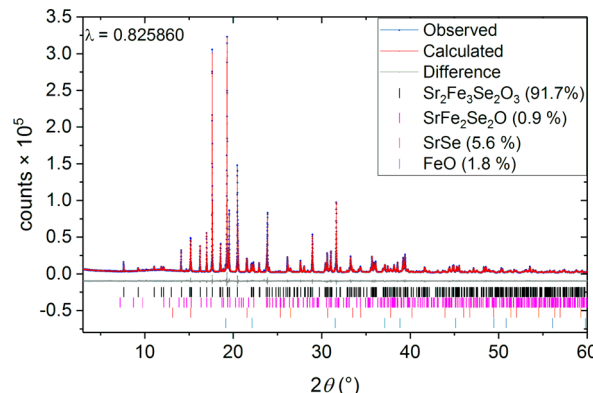


Figure 2. Rietveld refinement against the PXRD pattern (I11) of $\text{Sr}_2\text{Fe}_3\text{Se}_2\text{O}_3$ sample B taken at room temperature (this sample was intentionally prepared with a slight excess of SrSe in the reaction mixture, hence the presence of significant amounts of this phase in the sample).

reported phase with a large proportion of SrSe impurity. The synthesis was then modified by the inclusion of Fe_2O_3 and Fe to target $(\text{FeO})_x(\text{SrSe})_y$ compositions with $x > y$ to minimize impurities and infer the composition. Sample purity and Bragg peak asymmetry were found to vary greatly with the synthesis temperature, even with the correct compositional ratio of elements. Common impurities included SrSe , Fe_3O_4 , $\text{SrFe}_2\text{Se}_2\text{O}$, and FeO . Repeated annealing at 760 °C or below yielded a composition with higher levels of FeO or Fe_3O_4 impurity (~2–5% by mass), whereas repeated annealing above 760 °C yielded a product with higher levels of $\text{SrFe}_2\text{Se}_2\text{O}$ impurity (3–8% by mass). The highest purity samples were produced by placing the sealed crucible into a preheated furnace at 900 °C and leaving it to dwell for only 80

Table 1. Structural and Magnetic Information from Rietveld Refinement of $\text{Sr}_2\text{Fe}_3\text{Se}_2\text{O}_3$ ^a

	$\text{Sr}_2\text{Fe}_3\text{Se}_2\text{O}_3$ sample B			
instrument	I11		WISH	
T (K)	298	135	55	20
nuclear symmetry	$Pbam$ (55)	$Pbam$ (55)	$Pbam$ (55)	$Pbam$ (55)
a (Å)	7.8121(2)	7.8003(2)	7.7963(2)	7.7945(2)
b (Å)	10.23747(9)	10.2112(3)	10.2008(3)	10.1979(3)
c (Å)	3.99388(5)	3.99121(9)	3.98951(9)	3.9893(1)
V (Å ³)	319.413(7)	317.97(1)	317.18(1)	317.10(1)
density (g cm ⁻³)	5.70486(9)	5.7308(2)	5.7452(2)	5.7465(3)
R_{wp} (%)	5.22	4.10	4.55	4.61
χ^2	1.56	1.06	1.17	1.21
Sr–O × 2	2.6465(4)	2.617(2)	2.597(2)	2.609(2)
× 1	2.765(3)	2.787(4)	2.785(4)	2.784(4)
× 1	2.870(4)	2.876(4)	2.885(3)	2.874(5)
× 1	2.930(3)	2.904(4)	2.918(4)	2.915(4)
Sr–Se × 2	3.1253(7)	3.109(3)	3.113(2)	3.117(3)
× 2	3.1406(7)	3.137(2)	3.146(2)	3.155(3)
Fe1–O × 2	2.029(4)	2.011(3)	1.982(3)	1.992(4)
Fe1–Se × 4	2.7225(4)	2.738(2)	2.738(2)	2.708(2)
Fe2–O × 2	2.0059(3)	2.0084(4)	2.0076(3)	2.0078(4)
× 1	2.0878(9)	2.082(2)	2.103(1)	2.092(2)
Fe2–Se × 1	2.7659(10)	2.714(3)	2.721(3)	2.754(3)
× 1	2.8740(11)	2.905(3)	2.889(3)	2.870(3)
× 1	2.9017(11)	2.918(3)	2.894(2)	2.880(3)
regime	paramagnetic	paramagnetic	Fe2 ordered	Fe1 and Fe2 ordered
basis expansion of nuclear cell			[2,0,0], [0,1,0], [0,0,2]	[2,0,0], [0,2,0], [0,0,2]
origin			(-1/4,0,1/2)	(0,0,0)
magnetic symmetry (BNS)			$B_a b2_m$ (36.178) ^b	$I_a b$ (9.40) ^b
K vector			[1/2, 0, 1/2]	[1/2, 0, 1/2], [1/2, 1/2, 0]
Fe1 lspin along a , b , c (μ_B)				3.10(2), 1.34(7), 0
Fe1 total spin (μ_B)				3.38(3)
Fe2 lspin along a , b , c (μ_B)		0, 0, 3.01(1)	0.69(2), 0.59(5), 3.18(1)	
Fe2 total spin (μ_B)		3.01(1)	3.31(1)	

^aFurther details are given in the Supporting Information. ^bNonstandard settings of the magnetic space groups have been used to keep the directions of the lattice parameters consistent with the nuclear structure.

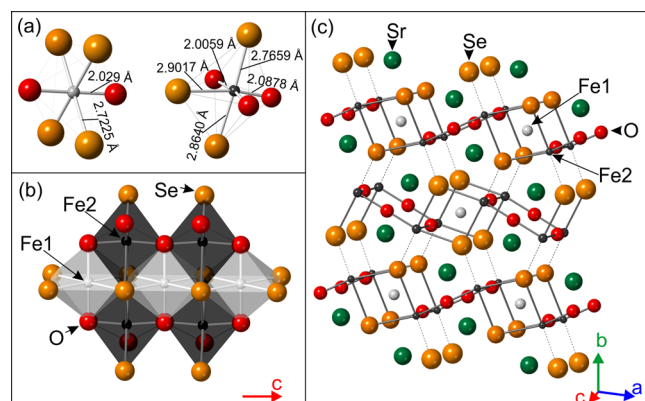


Figure 3. (a) Local coordination environments of the two iron sites; (b) connectivity of the Fe1 and Fe2 octahedra, described by Lai et al. as the necklace ladder. (c) Structure of $\text{Sr}_2\text{Fe}_3\text{Se}_2\text{O}_3$ showing the Fe2 bonding network. Solid bonds show linkages of Fe2 in the necklace ladder and 2-leg ladder that together form a layer described as a hybrid spin ladder,^{15,16} which joins to adjacent ladders through selenide vertexes (dashed bonds).

min before quenching in ice water. This is similar to the bulk synthesis reported by Lai et al., although their reaction was of a longer duration. This method produced samples with $\sim 1.1\%$

SrSe , 1.6% $\text{SrFe}_2\text{Se}_2\text{O}$, and 0.3% FeO by mass (sample A). The product was a gray powder, and the room temperature resistivity of a cold-pressed pellet of sample A was measured as $0.4 \text{ M}\Omega \text{ cm}$, suggesting insulating behavior. A second sample made by repeated annealing at 740°C in the intentionally slightly Sr,Se-rich stoichiometric ratio of 7Sr/10Fe/7Se/10O has also been used in this work (sample B), which contained only 0.9% $\text{SrFe}_2\text{Se}_2\text{O}$ and 1.2% FeO as well as a 5.6% SrSe impurity, which was readily treated as a second phase in the Rietveld refinement.

Structure Solution. The laboratory XRPD pattern of $\text{Sr}_2\text{Fe}_3\text{Se}_2\text{O}_3$ was initially indexed on an orthorhombic unit cell with dimensions of $7.81 \times 10.23 \times 3.99 \text{ \AA}$. Electron diffraction patterns on sample B confirmed the same unit cell and showed reflection conditions: $0kl$: $k = 2n$, $h0l$: $h = 2n$, $h00$: $h = 2n$, $0k0$: $k = 2n$, corresponding to the extinction symbol Pba -, allowing space groups $Pba2$ and $Pbam$. These diffractograms (Figure 1) showed well-formed spots with no evidence for streaking in the regions investigated. Structural solution was performed using charge flipping, as implemented in TOPAS Academic,²¹ with $Pbam$ symmetry imposed, using high-resolution PXRD data collected with the I11 instrument. The algorithm was successful in identifying the locations of all ions in the unit cell, allowing the identity of the ions on each site to be

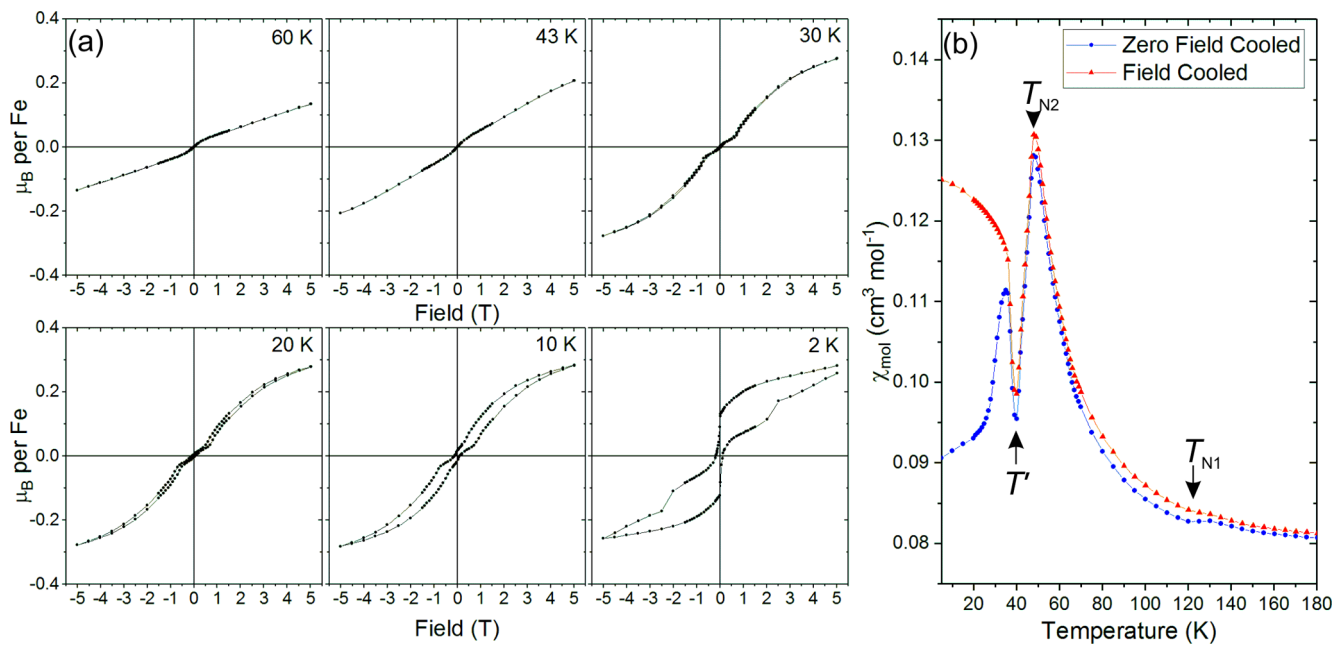


Figure 4. (a) Magnetisation isotherms measured by cooling sample B from 200 K in a +5T field to the measurement temperature and sweeping the field to -5 T and back to +5T. (b) Zero-field-cooled and field-cooled temperature dependence of the magnetic susceptibility of sample B measured in a 1000 Oe field.

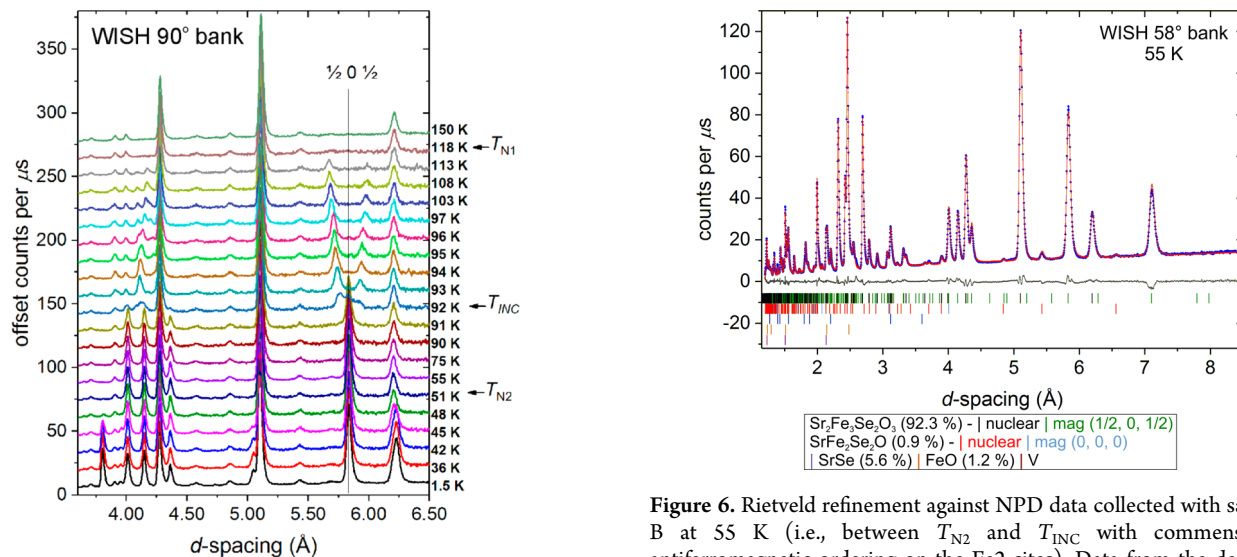


Figure 5. Evolution with temperature of the neutron powder diffraction patterns of $\text{Sr}_2\text{Fe}_3\text{Se}_2\text{O}_3$ sample A measured as a function of temperature. Data from the detector bank with a mean 2θ of 90° are shown.

subsequently deduced by comparison of their interionic distances with those in relevant binary compounds.

The structural model obtained from charge-flipping was confirmed and refined using Rietveld analysis. At this stage, the model was tested in space group $Pba2$, the other candidate space group that accounted for the systematic absences in the electron diffraction experiment. In reducing the symmetry from $Pbam$ to $Pba2$, site positions are allowed to refine freely along the z axis, a consequence of the lack of the center of inversion. No significant improvement to the fit or change in the atomic positions was observed on allowing this reduction of symmetry, so centrosymmetric $Pbam$ was chosen as the

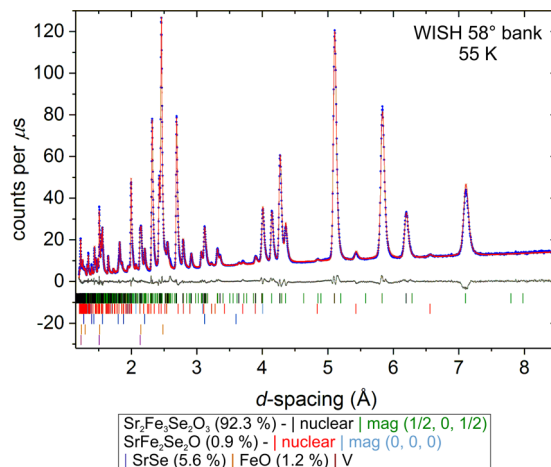


Figure 6. Rietveld refinement against NPD data collected with sample B at 55 K (i.e., between T_{N2} and T_{INC} with commensurate antiferromagnetic ordering on the Fe2 sites). Data from the detector bank with a mean 2θ of 58° are shown.

space group. During the course of our work, we became aware of the discovery of the isostructural compound $\text{Sr}_2\text{Co}_3\text{S}_2\text{O}_3$ ¹⁶ and the report of $\text{Sr}_2\text{Fe}_3\text{Ch}_2\text{O}_3$ ($\text{Ch} = \text{S}, \text{Se}$)¹⁵ in which single crystal X-ray diffraction confirmed this choice of space group $Pbam$. Rietveld refinement against synchrotron powder X-ray diffraction acquired using I11 achieved a good agreement to the data for sample B shown in Figure 2 and the data for sample A shown in Figure S1. The result of the structural analysis (Table 1) is entirely consistent with the report of Lai et al.¹⁵

The $\text{Sr}_2\text{Fe}_3\text{Se}_2\text{O}_3$ structure is shown in Figure 3. For further discussion of the structure, the reader is also referred to the works of Lai et al.^{15,16} The key features of the structure are as follows. There are two iron coordination environments shown in Figure 3a: Fe1 has a compressed *trans*- FeSe_2O_2 octahedral

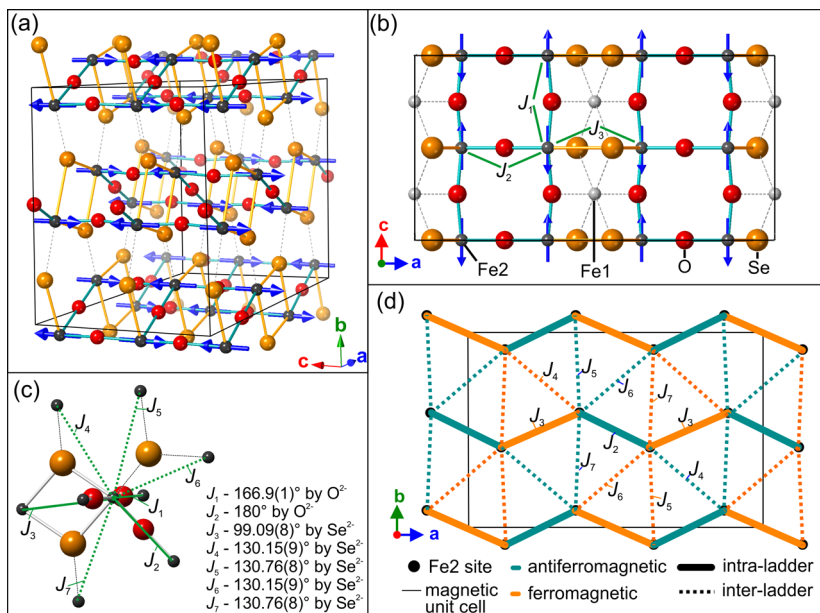


Figure 7. (a) Magnetic ordering scheme of the Fe2 sites between 51 (T_{N1}) and 92 K (T_{INC}) consisting of moments pointed along the c axis. Sr and Fe1 sites are not shown. (b) Arrangement of the Fe2 magnetic moments in the hybrid spin ladder. (c) Local environment of an Fe2 ion with J -couplings to seven other Fe2 ions that are mediated by a single anion: three of which are intraladder and four are interladder (d) schematic diagram of the magnetic ordering and couplings with colors indicating the relationships between neighboring spins. The magnetic moments in the diagram are directed in the plane along the c axis and are coupled antiferromagnetically (J_1) down that axis on all Fe2 sites. The unit cell shown is that of the magnetic cell, doubled along the a and c axes relative to the nuclear cell.

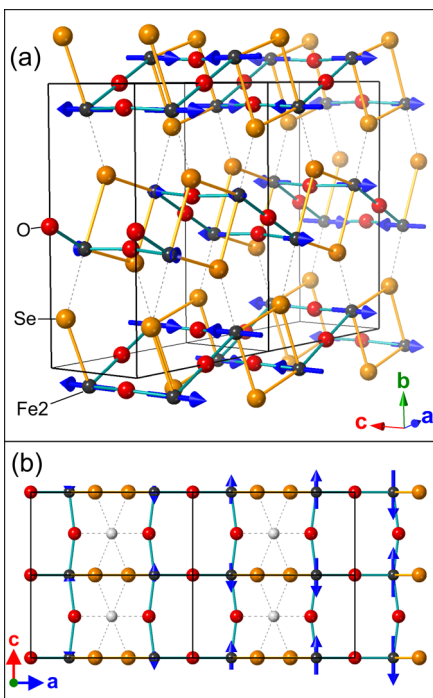


Figure 8. (a) Magnetic ordering scheme of the Fe2 sites between 120 (T_{N1}) and 92 K (T_{INC}) consisting of moments pointed along the c axis and an spin density wave incommensurate with the crystal structure in the a axis (propagation vector (a , 0, 1/2) with a = 0.42 in the case shown). (b) Arrangement of the Fe2 magnetic moments in the hybrid spin ladder. The unit cell shown is the nuclear cell. Fe1 sites are not shown in (a), and Sr sites are not shown in (a) or (b). See caption to Figure 7 for the convention on coloring of bonds.

environment with a multiplicity of 2 in the unit cell, while Fe2 has a distorted *mer*-FeSe₃O₃ octahedral environment with a

multiplicity of 4 in the unit cell. The two environments have complex interconnectivity shown in Figure 3b: Each *trans*-FeSe₄O₂ octahedron (Fe1) shares four faces (necessarily Se₂O₁) with *mer*-FeSe₃O₃ octahedra (Fe2) and is linked to two other *trans*-FeSe₄O₂ (Fe1) octahedra through Se₂ edges to form chains of the *trans*-FeSe₄O₂ (Fe1) polyhedra extending along the c axis. *mer*-FeSe₃O₃ octahedra (Fe2) connect to each other via Se₂ edges which are the same as those shared to form the chains of *trans*-FeSe₄O₂ (Fe1) octahedra extending along c (Figure 3b). The *mer*-FeSe₃O₃ (Fe2) octahedra are further linked along the c direction through *trans* O vertexes to two other *mer*-FeSe₃O₃ octahedra (Fe2). Lai et al.^{15,16} describe this motif (Figure 3b) extending along the c axis as a necklace ladder. The remaining O vertexes of the *mer*-FeSe₃O₃ (Fe2) octahedra join these necklace ladders along the a direction and the resulting double chains of O-vertex-linked *mer*-FeSe₃O₃ (Fe2) octahedra which extend along c are described as a 2-leg rectangular ladder.¹⁶ These connected ladders form a layer as shown by the solid bonds in Figure 3c that Lai et al. describe as a hybrid spin ladder.^{15,16} These hybrid ladders are joined together along the b axis by sharing of the remaining Se vertexes of the *mer*-FeSe₃O₃ (Fe2) octahedra as indicated by the dotted bonds in Figure 3c.

The coordination environments found in this compound should be compared with other transition metal oxide chalcogenides. The *trans*-FeSe₄O₂ coordination is found in La₂Fe₂Se₂O₉⁹ and relatives such as Sr₂Fe₂Se₂OF₂,²² Na₂Fe₂Se₂O₃,²³ and the phase of BaFe₂Se₂O synthesized at high pressure,²⁴ in which the polyhedra share faces producing layers containing Fe₂O sheets, an arrangement also found in chalcogenide and pnictide analogues with these structure types containing other transition metals^{25–28} and in the structurally related oxide sulfide Ca₂Fe_{2.6}S₂O₃.²⁹ Both polymorphs of La₂FeSe₂O₂ also display this coordination environment for Fe²⁺ ions with linking via shared selenide edges,³⁰ and this

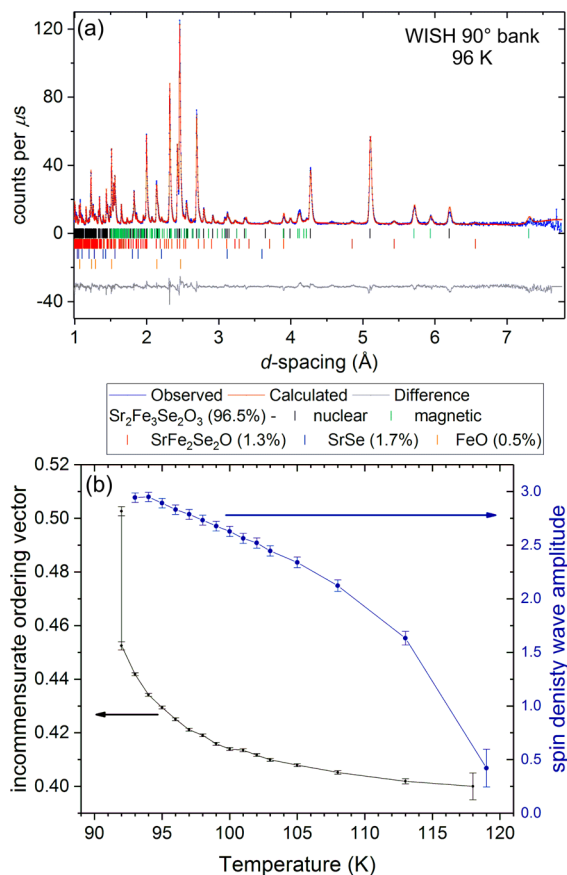


Figure 9. Rietveld refinement against WISH NPD data (data bank with a mean 2θ of 90°) of sample A at 96 K where the magnetic structure is incommensurate with the crystal structure (propagation vector $(a, 0, 1/2)$ with $a = 0.42$ in the case shown). (b) Plot of the amplitude of the spin density wave of the Fe2 sites and of the variable component a of the propagation vector $(a, 0, 1/2)$ against temperature.

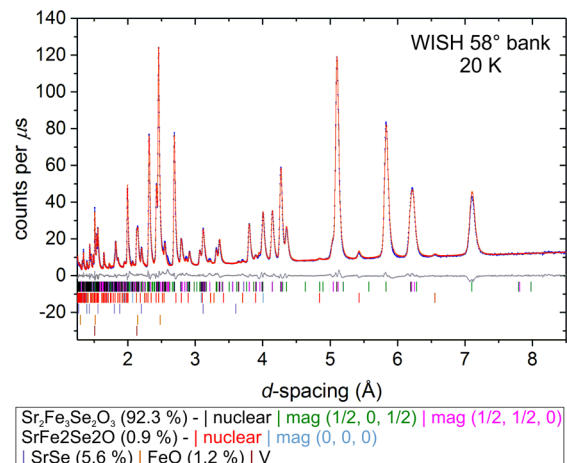


Figure 10. Rietveld refinement against NPD data collected with sample B at 20 K (below T_{N2} with both Fe sublattices ordered). Data from the detector bank with a mean 2θ of 58° are shown.

coordination environment and mode of connection is also found in $\text{La}_5\text{V}_3\text{O}_7\text{S}_6$.³¹ As discussed by Lai et al. in the original report of $\text{Sr}_2\text{Co}_3\text{S}_2\text{O}_3$,¹⁶ the *mer*- $[\text{MX}_3\text{O}_3]$ octahedral environment (M = transition metal; X = nonoxide ion) is rare,

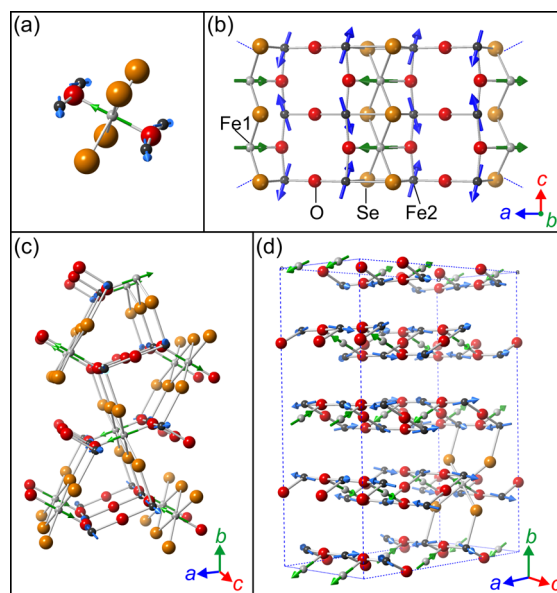


Figure 11. Magnetic structure of $\text{Sr}_2\text{Fe}_3\text{Se}_2\text{O}_3$ observed between 1.5 and 50 K (T_{N2}). (a) the local environment of the Fe1 moment relative to the nearest neighbor Fe2 sites. (b) Arrangement of Fe1 and Fe2 moments in the spin hybrid ladders (compare with Figure 7b). (c) Arrangement of moments between ladders. (d) magnetic unit cell below T_{N2} , which is a $2a \times 2b \times 2c$ expansion relative to the nuclear cell (see Table S6). Sr and most Se sites not shown in (d) for clarity.

although it has been reported for TiS_3O_3 octahedra in $\text{La}_6\text{Ti}_2\text{S}_8\text{O}_5$.³²

Magnetometry. Our magnetic susceptibility measurements show transitions consistent with those observed using magnetometry and heat capacity measurements by Lai et al.¹⁵ In what follows, we adopt their notation. The transitions are shown in Figure 4b at ~ 125 K (T_{N1}), 50 K (T_{N2}), and 40 K (T'). T_{N1} coincides approximately with the Verwey transition of Fe_3O_4 , and while only 0.05% of this phase (below the detection limit of bulk diffraction measurements) would be required to produce such a transition in the magnetization, the heat capacity measurements of Lai et al.¹⁵ show that this feature is associated with the bulk of the sample. Figure 4a shows a change in the shape of the hysteresis loops, obtained after field-cooling from room temperature at 5 T, on passing through the 50 K (T_{N2}) and 40 K (T') transitions. Below T' , a metamagnetic transition appears at about 0.6 T in the magnetization isotherm. This feature persists to lower temperatures and is evident in the virgin curve of the magnetization isotherm at 2 K obtained after zero-field-cooling in the report of Lai et al.¹⁵ In our field-cooled (5 T) isotherm at 2 K, a higher-field feature is evident above 2 T which was also observed in the hysteresis loop of Lai et al.¹⁵ The behavior suggests that there may be a field-dependence to the magnetic ordering which would require neutron diffraction investigations beyond the scope of those performed here.

Neutron Powder Diffraction. Variable-temperature NPD measurements (Figure 5) were carried out on both samples A and B on warming. Sample A was measured in narrow temperature steps from 1.5 to 150 K, while diffraction patterns with better statistics were collected on sample B at 20, 55, 97, and 135 K corresponding to key ordered states. Rietveld refinements against data from both samples produced identical models for the magnetic ordering. On cooling, we observe magnetic ordering transitions as follows. Below 118 K

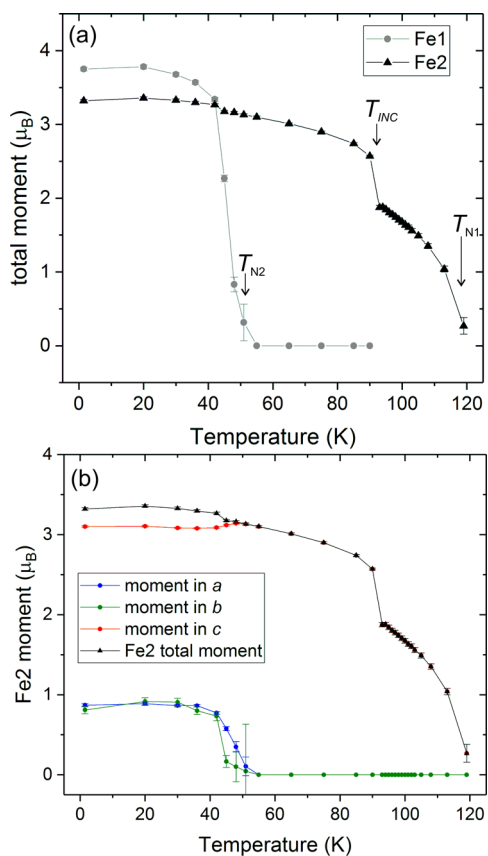


Figure 12. Evolution of (a) the total ordered moments on the two Fe sites and (b) the evolution of the components of the Fe2 moments showing the change in orientation that coincides with the onset of long-range ordering of the Fe1 moments at T_{N2} . The kink in the magnitude of the Fe2 moment at T_{INC} is consistent with the first order character of the lock-in transition.

(equated with T_{N1}), magnetic Bragg peaks begin to appear. On cooling further, these peaks shift remarkably in *d*-spacing until 92 K is reached (Figure 5). We identify this temperature as a fourth magnetic transition for this compound which is not evident in the magnetic susceptibility measurements. We give this the symbol T_{INC} because it is associated with the transition between commensurate and incommensurate magnetic ordering as described below. Below 51 K (T_{N2}), an additional set of magnetic reflection appears, which increase sharply in intensity as the temperature is lowered, as can be seen in the change in intensity of the peak at 3.8 Å between 48 and 42 K in Figure 5.

Analysis of the commensurate reflections was performed using the ISODISTORT software,³³ coupled with Rietveld refinement in Topas Academic v6.¹⁹ Rietveld refinement of the incommensurate magnetic structure was performed using FullProf.³⁴

Magnetic scattering in all diffraction patterns above $T_{N2} = 51$ K could be accounted for solely by ordering on one of the Fe sites. In principle the magnetic contribution to the Bragg scattering alone does not allow us to distinguish whether the Fe1 or the Fe2 site is responsible. However, the Fe2/Fe1 ratio of 2:1 enabled us to deduce, from the size of the ordered moment, that the Fe2 site (the *mer*-Fe₃O₃ site which accounts for two-thirds of the iron sites) must be the one ordered in this regime (with an ordered moment of 3.04(1) μ_B at 55 K); otherwise, the less numerous Fe1 sites would each carry an ordered moment of 4.75(2) μ_B at 55 K, which exceeds

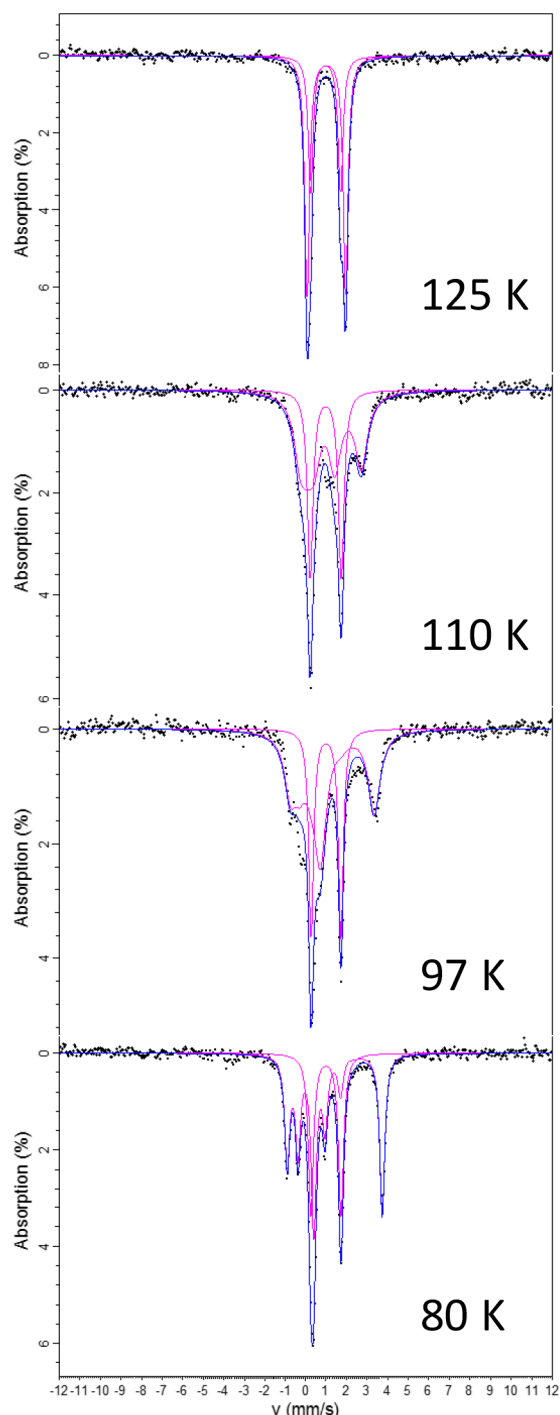


Figure 13. Mössbauer spectra measured through the transitions T_{N1} and T_{INC} . Isomer shift relative to room temperature thin α -Fe foil.

the maximum saturated value expected for Fe^{2+} . This result is consistent with the Mössbauer data (see below). We first consider the magnetic structure that pertains between T_{N2} (51 K) and T_{INC} (92 K). This can be accounted for (Figure 6 shows the refinement against 55 K data) by commensurate ordering of the Fe2 moments with propagation vector $k = (1/2, 0, 1/2)$. Trials of the possible magnetic ordering modes in the expanded unit cell gave a good fit to the data with a combination of $m\mathbf{U}_2(\xi_1, 0)$ modes (following the notation^{35,36} of Miller and Love used in ISODISTORT). This may be described in the magnetic space group $B_a b2_1 m$ (36.178) (BNS

Table 2. Summary of Mössbauer Parameters of Fit Components, Relative to Room Temperature α -Fe

temp (K)	site	δ (mm s^{-1})	ΔE_Q (mm s^{-1})	η	B_{hf} (T)	HWHM (mm s^{-1})	area (%)	reduced χ^2
125	Fe1	0.96	1.46			0.15	37	0.784
	Fe2	1.00	1.88			0.14	63	
110	Fe1	0.97	1.52			0.17	37	1.350
	Fe2	1.06	1.83 ^a	0.7 ^a	4.16	0.36	63	
97	Fe1	0.98	1.45			0.14	34	2.190
	Fe2	1.00	1.83 ^a	0.7 ^a	8.49	0.35	66	
80	Fe1	0.98	1.47			0.15	34	0.840
	Fe2	1.03	1.71	0.7	11.11	0.15	66	
± 1		± 0.02	± 0.02			± 0.5	± 0.01	± 1

^aQuadrupole splitting, ΔE_Q , and asymmetry, η , fixed in the incommensurate region.

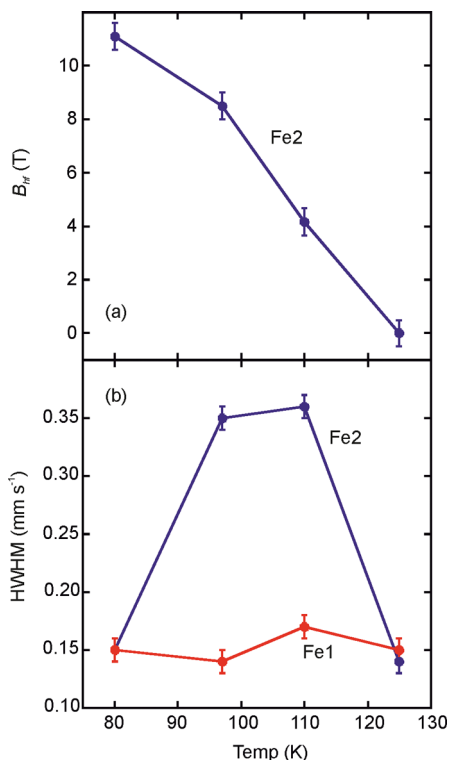


Figure 14. (a) The evolution of the mean hyperfine field, B_{hf} for the Fe2 sites on cooling through T_{N1} and T_{INC} . (b) The evolution of the linewidths (expressed as half-width at half-maximum (HWHM)) for the Fe1 and Fe2 signals on cooling through T_{N1} and T_{INC} . The broader widths in the region of the incommensurate spin density wave order of the Fe2 moments are ascribed to the range of hyperfine fields experienced by these sites. See Table 2.

notation).³⁷ The ordering scheme is as shown in Figure 7, in which the moments are directed along the c axis with antiferromagnetic coupling (J_1). In the direction of the a axis, the moments are antiferromagnetically aligned along the vertex-sharing 180° Fe(2)–O–Fe(2) pathways (J_2) and ferromagnetically aligned along the 99° Fe(2)–Se–Fe(2) pathways (J_3) resulting from edge sharing. These three J_1 couplings in the ac plane occur in the hybrid spin ladders described by Lai et al.¹⁵ It is these intraladder interactions that appear to dominate the magnetic ordering scheme between T_{N2} and T_{INC} . The alignment of spins by the interladder couplings (J_4 – J_7) exhibits an inherent frustration: According to the refined magnetic structure, for half the Fe2 ions J_4 is ferromagnetic, but J_5 , J_6 , and J_7 are antiferromagnetic. For the other half of the Fe2 ions J_4 is antiferromagnetic, but J_5 , J_6 , and

J_7 are ferromagnetic. The ordering is summarized in the schematic in Figure 7d.

We note that the resulting magnetic space group is polar, indicating that the magnetic transition at T_{INC} breaks the spatial inversion symmetry. Indeed, the magnetic order, which transforms as the $mU_2(\xi_1, 0)$ irreducible representation, couples a displacive distortion with the $\Gamma_4^-(\sigma)$ symmetry through the linear quadratic invariant $\sigma\xi_1^2$ in the free energy. This lattice distortion can give rise to a net dipolar moment in the structure, and it is probably the origin of the frustration release in the interladder couplings (J_4 – J_7 in Figure 7).

On warming through T_{INC} , the magnetic Bragg peaks on a propagation vector (1/2, 0, 1/2) develop satellite peaks which can be indexed to a propagation vector of (1/2 – δ , 0, 1/2) ($0 \leq \delta \leq 0.1$). The transition appears sharp and first-order, with solely commensurate ordering observed at 91 K, coexistence of the commensurate and incommensurate phases observed at 92 K (shown in Figure S2) and solely incommensurate ordering observed at 93 K. The satellite peaks diverge from the commensurate ordering vector above 93 K as shown for the 1/2 0 1/2 reflection in Figure 5, appearing at positions $1/2 \pm \delta$ 0 1/2 with δ increasing from 0 to a maximum of 0.10 before long-range order is lost at T_{N1} . Our model for the incommensurate magnetic structure is still described by spins directed along the c axis, with antiferromagnetic alignment (J_1). Magnetic couplings in the a axis still have net antiferromagnetic alignment along the 180° oxide linkages (J_2) and net ferromagnetic alignment along the 99° selenide linkages (J_3); however, there is a modulation in the size of the ordered moment along a as shown in Figure 8. The occurrence of this incommensurate magnetic structure is presumably a response to the inherent frustration of the interlayer interactions (J_4 – J_7) in the commensurate structure below T_{INC} , shown by the dotted lines in Figure 7c: The modulation in each layer is out of phase with that in the adjacent layer, such that when the moment is at a maximum in one layer it is at a minimum in the layer below. Numerous systems are known where frustration of magnetic interactions results in the adoption of a modulated magnetic structure.^{38–41} Attempts to model the magnetic scattering using a cycloidal magnetic structure produced poor fits (see Figure S8).

Rietveld refinement against the neutron diffraction pattern at 96 K is shown in Figure 9a. The incommensurate magnetic structure is described within the $Pbam1'(a01/2)000s$ super-space group corresponding to the action of the $ma3$ irreducible representation of the parent space group and can be described as a spin density wave with amplitude $\sim 3.0 \mu_B$ at 95 K. The transition at T_{INC} is a lock-in on cooling from the incommensurate propagation vector to the commensurate (1/

2 0 1/2) value with a locking of the origin (corresponding to a locking of the phase of the sine wave) along the propagation vector direction to the value $1/8 + n/2$, where n is an integer number, resulting in the $B_a b2_1 m$ magnetic space group. There appears to be no discernible signature of this transition in the susceptibility measurements.

A second set of magnetic reflections appears below T_{N2} (51 K), which index on a propagation vector $k = (1/2, 1/2, 0)$. These arise from the long-range ordering of the moments on the Fe1 sites combined with the existing magnetic ordering of the Fe2 sites, this gives an overall magnetic unit cell of $2a \times 2b \times 2c$ relative to the structural cell. ISODISTORT was used to test ordering schemes for the Fe1 moments that might contribute to the additional reflections observed below T_{N2} , with k point S ($k = 1/2, 1/2, 0$), for which it was found the majority of the new magnetic scattering could be accounted for by a combination of $mS3+S4+(\epsilon_1, \epsilon_2)$ modes; however, it was not possible to fit the new magnetic intensities (Figure 10) which occur below T_{N2} using solely a combination of the Fe1 magnetic ordering modes without serious discrepancies. Allowing the already-ordered Fe2 moments to reorient so that they would contribute to the intensity of these new magnetic Bragg peaks that emerge below T_{N2} gave a much improved fit, with better visual agreement and a lowered R_{wp} from 7.8 to 4.6%. In the overall fit the Fe1 moments lie along the Fe1–O bonds in the ab plane, which was also the conclusion of Lai et al.¹⁵ from fitting of their Mössbauer data, and this and their ferromagnetic alignment via sharing of Se_2 edges is consistent with the orientation of moments in the magnetic structure of $Sr_2Fe_2S_2OF_2$.⁴² The Fe2 moments that were already ordered above T_{N2} remain principally directed along the c axis with the $mU2$ ordering scheme; however, to fully account for the magnetic intensities below T_{N2} , they acquire a canting in the ab plane described by a combination of $mS3+S4+$ modes. A comparison of the fit with and without this Fe2 site canting is given in the Figure S3. This rearrangement of the spins becomes established at 40 K and may be associated with the T' transition in heat capacity measurements of Lai et al.¹⁵ The canting puts the Fe2 moments in a plane with their nearest Fe1–O bond and the corresponding Fe1 moment, with antiferromagnetic alignment between each of the Fe1 moments and the Fe2 moments canting as shown in Figure 11a. The ordering scheme thus derived is purely antiferromagnetic, and can be described in the I_{ab} magnetic space group in a $2a_{\text{nucl}} \times 2b_{\text{nucl}} \times 2c_{\text{nucl}}$ cell (Table S6). In light of the weak ferromagnetic component of the susceptibility evident in the magnetometry below T' at 40 K, ordering modes which gave a net ferromagnetic canting of one or both sets of spins were attempted, but none gave improvement to the fit, suggesting that the zero-field magnetic structure (i.e., as measured in the NPD experiment) is purely antiferromagnetic. Moreover, the determined magnetic space group does not allow any ferromagnetic moment in any crystallographic direction. Indeed, the magnetization versus field curves shown in Figure 4 are close to linear at low fields, which is consistent with AFM ordering without an applied field.

To explain the canting of the Fe2 sublattice with the $mS3+S4+(\epsilon_1, \epsilon_2)$ modes, it is necessary to take into consideration a nuclear distortion with the right symmetry to allow a trilinear invariant in the free energy, coupling the two magnetic distortions. To conserve the translational symmetry of the parent structure, the nuclear distortion needs to have a propagation vector $q = (0 1/2 1/2)$, the T point of the first

Brillouin zone, and to transform as the $T2$ irreducible representation with order parameter direction $P(\delta_1, \delta_2)$. This allows us to derive a trilinear invariant $a\xi_1(\epsilon_1\delta_1 + \epsilon_2\delta_2) + b\xi_1(\epsilon_1\delta_2 - \epsilon_2\delta_1)$ describing the coupling, mediated by the $T2(\delta_1, \delta_2)$, between the magnetic $mU_2(\xi_1, 0)$ and $mS3+S4+(\epsilon_1, \epsilon_2)$ distortions. Any monoclinic nuclear distortion was outside the resolution of the WISH diffractometer, and we did not observe any superstructure reflections consistent with $q = (0 1/2 1/2)$. We used the X-ray diffractometer ID22 at the ESRF to investigate whether the magnetic ordering at T_{N2} gives rise to a small monoclinic distortion of the nuclear cell or the presence of $0 1/2 1/2$ peaks that might be associated with the T' transition in the heat capacity data of Lai et al.¹⁵ Our measurement at 5 K showed no apparent symmetry lowering distortion (Figure S4), but a careful observation of the diffraction pattern indicated the presence of a very weak reflection, not present at ambient temperatures, that could be indexed as the $0 5/2 1/2$ reflection (Figure S5). Even if this reflection is statistically significant, its spurious nature cannot be excluded, but its position and the propagation vector are consistent with the symmetry analysis. A refinement with the distorted monoclinic symmetry Im is not possible due to the weak character of the distortion (i.e., the low intensity of the proposed $0 5/2 1/2$ reflection) and the high number of free parameters. Even considering this extra nuclear distortion, on the ground state magnetic space group, the weak ferromagnetic moment is still not allowed from the resulting symmetry. Note that we needed to use an attenuated beam on ID22 to avoid sample heating when performing this experiment: With the full intensity beam sample heating was evident as had been observed and described in measurements down to 75 K by Lai et al. on the same instrument (see their Figure S4).¹⁵ Figure 12 summarizes the evolution of the ordered moments over the entire temperature range.

Mössbauer Spectroscopy. The temperature dependence of the Mössbauer spectra has been described and interpreted by Lai et al.¹⁵ Here we show the evolution of the spectra in the region from just above T_{N1} to just below T_{INC} spanning the region where the magnetic ordering of the Fe2 moments is incommensurate and the Fe1 moments do not participate in long-range order. The data and fits in Figure 13 show the onset of magnetic order between 125 and 110 K and the evolution to 80 K, below T_{INC} . At 125 K (Figure 13) in the paramagnetic region, the data are modeled by two doublets. The more numerous Fe2 moments produce a doublet with a chemical shift (relative to a thin Fe foil) of $\delta = 1.001(2)$ mm s⁻¹ and with a quadrupole splitting of $\Delta E_Q = 1.897(8)$ mm s⁻¹. The remaining doublet is ascribed to the Fe1 moments ($\delta = 0.963(4)$ mm s⁻¹; $\Delta E_Q = 1.46(1)$ mm s⁻¹). As magnetic ordering occurs, the majority signal due to the Fe2 sites is described by a sextet confirming that it is the Fe2 moments that are participating in long-range magnetic order below T_{N1} (see the potential ambiguity described above in the analysis of the NPD data). At 80 K (Figure 13), below T_{INC} , the signal due to these Fe2 moments is described by a highly asymmetric sextet arising from the local magnetic field, B_{hf} due to the magnetic ordering and the quadrupole splitting due to the asymmetric coordination environment.⁴³ The minority Fe1 signal persists as a quadrupole doublet. In the region between T_{N1} and T_{INC} where the NPD data show incommensurate magnetic ordering of the Fe2 moments, the Fe2 sextet in the Mössbauer spectrum exhibits very broad lines. The data in this region (110 and 97 K in Figure 13; fitting parameters are given

in Table 2) were modeled using a quadrupole splitting similar to that used in the paramagnetic region above T_{NI} and in the commensurately ordered region below T_{INC} and a single value for the local magnetic field that steadily increased with decreasing temperature (Figure 14a), but they required much broader line widths in this region (Figure 14b) consistent with the spin density wave type order reflecting a wide range of local magnetic fields experienced by the ensemble of Fe2 ions. For discussion of the Mössbauer spectra at lower temperatures where Fe1 undergoes magnetic ordering the reader is referred to the data and analysis of Lai et al.¹⁵

CONCLUSIONS

$Sr_2Fe_3Se_2O_3$, with two unusual and highly anisotropic environments for Fe^{2+} ions, shows a complex succession of magnetic ordering transitions. Neutron powder diffraction measurements unveil the origin of the complexity in the magnetic susceptibility and Mössbauer spectra previously described¹⁵ and reveal an additional region of magnetic behavior where the onset of long-range magnetic ordering on one of the Fe sublattices (Fe2) on cooling results first of all in an incommensurate region of long-range order, presumably driven by frustration of some of the weaker exchange interactions. The lowest temperature magnetic structure is dictated by the interactions between the two sublattices of long-range-ordered Fe moments. Given the complexity of the magnetic structures found for compounds composed of these highly anisotropic transition metal coordination environments,^{26,42} there is scope for tuning the details of the exchange interactions by chemical substitution on the transition metal, chalcogenide, and electropositive metal sites.

ASSOCIATED CONTENT

Supporting Information

The Supporting Information is available free of charge on the ACS Publications website at DOI: [10.1021/acs.inorgchem.8b01542](https://doi.org/10.1021/acs.inorgchem.8b01542).

Further Rietveld refinements and diffractograms, tables of refinement results and further discussion of the magnetic models (PDF)

AUTHOR INFORMATION

Corresponding Author

*E-mail: simon.clarke@chem.ox.ac.uk.

ORCID

Fabio Orlandi: [0000-0001-6333-521X](https://orcid.org/0000-0001-6333-521X)

Simon J. Clarke: [0000-0003-4599-8874](https://orcid.org/0000-0003-4599-8874)

Notes

The authors declare no competing financial interest.

ACKNOWLEDGMENTS

S. J. Cassidy prepared the samples and performed the diffraction and magnetometry measurements. F.O., P.M., and S. J. Cassidy measured and interpreted the NPD data. J.H. performed and interpreted the electron diffraction measurements. A.S. and P.A.B. performed and interpreted the Mössbauer spectroscopy measurements. S. J. Cassidy and S. J. Clarke conceived the project and wrote the paper with input from all co-authors. We acknowledge the financial support of the EPSRC (Grants EP/I017844/1, EP/P018874/1, and EP/M020517/1), and the Leverhulme Trust (RPG-2014-221). We

thank the ESTEEM2 network for enabling the electron microscopy investigations, the ISIS facility for the award of beamtime on WISH (RB1610357), and the Diamond Light Source Ltd. for the award of beam time on I11 (allocation EE13284). We thank Dr. C. Murray, Dr. S. Day and Dr. A. Baker for assistance on I11 and Dr. M. Coduri and Dr. A. N. Fitch for assistance on ID22.

REFERENCES

- Hiramatsu, H.; Kamihara, Y.; Yanagi, H.; Ueda, K.; Kamiya, T.; Hirano, M.; Hosono, H. Layered mixed-anion compounds: Epitaxial growth, active function exploration, and device application. *J. Eur. Ceram. Soc.* **2009**, *29*, 245–253.
- Ueda, K.; Inoue, S.; Hirose, S.; Kawazoe, H.; Hosono, H. Transparent p-type semiconductor: LaCuOS layered oxysulfide. *Appl. Phys. Lett.* **2000**, *77*, 2701–2703.
- Scanlon, D. O.; Watson, G. W. $(Cu_2S_2)(Sr_3Sc_2O_5)$ -A layered, direct band gap, p-type transparent conducting oxycalcogenide: A theoretical analysis. *Chem. Mater.* **2009**, *21*, 5435–5442.
- Zhao, L. D.; Berardan, D.; Pei, Y. L.; Byl, C.; Pinsard-Gaudart, L.; Dragoe, N. $Bi_{1-x}Sr_xCuSeO$ oxyseLENides as promising thermoelectric materials. *Appl. Phys. Lett.* **2010**, *97*, 092118.
- Kamihara, Y.; Watanabe, T.; Hirano, M.; Hosono, H. Iron-Based Layered Superconductor $La[O_{1-x}F_x]FeAs$ ($x = 0.05–0.12$) with $T_c = 26$ K. *J. Am. Chem. Soc.* **2008**, *130*, 3296–3297.
- Hsu, F.-C.; Luo, J.-Y.; Yeh, K.-W.; Chen, T.-K.; Huang, T.-W.; Wu, P. M.; Lee, Y.-C.; Huang, Y.-L.; Chu, Y.-Y.; Yan, D.-C.; Wu, M.-K. Superconductivity in the PbO-type structure -FeSe. *Proc. Natl. Acad. Sci. U. S. A.* **2008**, *105*, 14262–14264.
- Sun, H.; Woodruff, D. N.; Cassidy, S. J.; Allcroft, G. M.; Sedlmaier, S. J.; Thompson, A. L.; Bingham, P. A.; Forder, S. D.; Cartenet, S.; Mary, N.; Ramos, S.; Foronda, F. R.; Williams, B. H.; Li, X.; Blundell, S. J.; Clarke, S. J. Soft chemical control of superconductivity in lithium iron selenide hydroxides $Li_{1-x}Fe_x(OH)Fe_{1-y}Se$. *Inorg. Chem.* **2015**, *54*, 1958–1964.
- Clarke, S. J.; Adamson, P.; Herkelrath, S. J. C.; Rutt, O. J.; Parker, D. R.; Pitcher, M. J.; Smura, C. F. Structures, Physical Properties, and Chemistry of Layered Oxycalcogenides and Oxypnictides. *Inorg. Chem.* **2008**, *47*, 8473–8486.
- Mayer, J. M.; Schneemeyer, L. F.; Siegrist, T.; Waszczak, J. V.; Van Dover, B. New Layered Iron-Lanthanum-Oxide-Sulfide and -Selenide Phases: $Fe_2La_2O_3E_2$ ($E = S, Se$). *Angew. Chem., Int. Ed. Engl.* **1992**, *31*, 1645–1647.
- Huh, S.; Prots, Y.; Adler, P.; Tjeng, L. H.; Valldor, M. Synthesis and Characterization of Frustrated Spin Ladders $SrFe_2S_2O$ and $SrFe_2Se_2O$. *Eur. J. Inorg. Chem.* **2015**, *2015*, 2982–2988.
- Cassidy, S. J.; Batuk, M.; Batuk, D.; Hadermann, J.; Woodruff, D. N.; Thompson, A. L.; Clarke, S. J. Complex Microstructure and Magnetism in Polymorphic CaFeSeO. *Inorg. Chem.* **2016**, *55*, 10714–10726.
- Han, F.; Wang, D.; Malliakas, C. D.; Sturza, M.; Chung, D. Y.; Wan, X.; Kanatzidis, M. G. (CaO)(FeSe): A Layered Wide-Gap Oxycalcogenide Semiconductor. *Chem. Mater.* **2015**, *27*, 5695–5701.
- Lai, K. T.; Komarek, A. C.; Fernández-Díaz, M. T.; Chang, P. S.; Huh, S.; Rosner, H.; Kuo, C. Y.; Hu, Z.; Pi, T. W.; Adler, P.; Ksenofontov, V.; Tjeng, L. H.; Valldor, M. Canted Antiferromagnetism on Rectangular Layers of Fe^{2+} in Polymorphic CaFeSeO. *Inorg. Chem.* **2017**, *56*, 4271–4279.
- Delacotte, C.; Pérez, O.; Pautrat, A.; Berthebaud, D.; Hébert, S.; Suard, E.; Pelloquin, D.; Maingan, A. Magnetodielectric Effect in Crystals of the Noncentrosymmetric CaOFeS at Low Temperature. *Inorg. Chem.* **2015**, *54*, 6560–6565.
- Lai, K. T.; Adler, P.; Prots, Y.; Hu, Z.; Kuo, C.-Y.; Pi, T.-W.; Valldor, M. Successive Phase Transitions in Fe^{2+} Ladder Compounds $Sr_2Fe_3Ch_2O_3$ ($Ch = S, Se$). *Inorg. Chem.* **2017**, *56*, 12606–12614.

(16) Lai, K. T.; Valldor, M. Coexistence of spin ordering on ladders and spin dimer formation in a new-structure-type compound $\text{Sr}_2\text{Co}_3\text{S}_2\text{O}_3$. *Sci. Rep.* **2017**, *7*, 43767.

(17) Thompson, S. P.; Parker, J. E.; Potter, J.; Hill, T. P.; Birt, A.; Cobb, T. M.; Yuan, F.; Tang, C. C. Beamline I11 at Diamond: A new instrument for high resolution powder diffraction. *Rev. Sci. Instrum.* **2009**, *80*, 075107.

(18) Chapon, L. C.; Manuel, P.; Radaelli, P. G.; Benson, C.; Perrott, L.; Ansell, S.; Rhodes, N. J.; Raspino, D.; Duxbury, D.; Spill, E.; Norris, J. WISH: The New Powder and Single Crystal Magnetic Diffractometer on the Second Target Station. *Neutron News* **2011**, *22*, 22–25.

(19) Coelho, A. A. *TOPAS Academic*, version 5; Coelho Software: Brisbane, Queensland, Australia, 2012.

(20) Kovats, T. A.; Walker, J. C. Mössbauer absorption in Fe^{57} in metallic iron from the Curie point to the γ - δ Transition. *Phys. Rev.* **1969**, *181*, 610–618.

(21) Rancourt, D. *Recoil: Mössbauer Spectral Analysis Software*; Mössbauer Group: Ottawa, Ontario, Canada, 1998.

(22) Kabbour, H.; Janod, E.; Corraze, B.; Danot, M.; Lee, C.; Whangbo, M.-H.; Cario, L. Structure and Magnetic Properties of Oxychalcogenides $\text{A}_2\text{Fe}_2\text{OQ}_2$ ($\text{A} = \text{Sr, Ba}$; $\text{Q} = \text{S, Se}$) with Fe_2O Square Planar Layers Representing an Antiferromagnetic Checkerboard Spin Lattice. *J. Am. Chem. Soc.* **2008**, *130*, 8261–8270.

(23) He, J. B.; Wang, D. M.; Shi, H. L.; Yang, H. X.; Li, J. Q.; Chen, G. F. Synthesis, structure, and magnetic properties of the layered iron oxychalcogenide $\text{Na}_2\text{Fe}_2\text{Se}_2\text{O}$. *Phys. Rev. B: Condens. Matter Mater. Phys.* **2011**, *84*, 205212.

(24) Takeiri, F.; Matsumoto, Y.; Yamamoto, T.; Hayashi, N.; Li, Z.; Tohyama, T.; Tassel, C.; Ritter, C.; Narumi, Y.; Hagiwara, M.; Kageyama, H. High-pressure synthesis of the layered iron oxyselenide $\text{BaFe}_2\text{Se}_2\text{O}$ with strong magnetic anisotropy. *Phys. Rev. B: Condens. Matter Mater. Phys.* **2016**, *94*, 184426.

(25) Wang, C.; Tan, M. Q.; Feng, C. M.; Ma, Z. F.; Jiang, S.; Xu, Z. A.; Cao, G. H.; Matsubayashi, K.; Uwatoko, Y. $\text{La}_2\text{Co}_2\text{Se}_2\text{O}_3$: A quasi-two-dimensional mott insulator with unusual cobalt spin state and possible orbital ordering. *J. Am. Chem. Soc.* **2010**, *132*, 7069–7073.

(26) Free, D. G.; Withers, N. D.; Hickey, P. J.; Evans, J. S. O. Synthesis, Structure and Properties of Several New Oxychalcogenide Materials with the General Formula $\text{A}_2\text{O}_2\text{M}_2\text{OSe}_2$ ($\text{A} = \text{La–Sm}$, $\text{M} = \text{Fe, Mn}$). *Chem. Mater.* **2011**, *23*, 1625–1635.

(27) Ni, N.; Climent-Pascual, E.; Jia, S.; Huang, Q.; Cava, R. J. Physical properties and magnetic structure of the layered oxyselenide $\text{La}_2\text{O}_3\text{Mn}_2\text{Se}_2$. *Phys. Rev. B: Condens. Matter Mater. Phys.* **2010**, *82*, 214419.

(28) Valldor, M.; Merz, P.; Prots, Y.; Schnelle, W. Bad-Metal-Layered Sulfide Oxide $\text{CsV}_2\text{S}_2\text{O}$. *Eur. J. Inorg. Chem.* **2016**, *2016*, 23–27.

(29) Zhang, H.; Wu, X.; Li, D.; Jin, S.; Chen, X.; Zhang, T.; Lin, Z.; Shen, S.; Yuan, D.; Chen, X. $\text{Ca}_2\text{O}_3\text{Fe}_{2.6}\text{S}_2$: an antiferromagnetic Mott insulator at proximity to bad metal. *J. Phys.: Condens. Matter* **2016**, *28*, 145701.

(30) Nitsche, F.; Niklaus, R.; Johrendt, D. New Polymorphs of $\text{RE}_2\text{FeSe}_2\text{O}_2$ ($\text{RE} = \text{La, Ce}$). *Z. Anorg. Allg. Chem.* **2014**, *640*, 2897–2902.

(31) Dugué, J.; Tien, V.; Laruelle, P. Structure de l’oxy sulfure de lanthane et de vanadium, $\text{La}_5\text{V}_3\text{O}_7\text{S}_6$. *Acta Crystallogr., Sect. C: Cryst. Struct. Commun.* **1985**, *41*, 1146–1148.

(32) Cody, J. A.; Ibers, J. A. Synthesis and Characterization of the New Rare-Earth/Transition-Metal Oxy sulfides $\text{La}_6\text{Ti}_2\text{S}_8\text{O}_5$ and $\text{La}_4\text{Ti}_3\text{S}_4\text{O}_8$. *J. Solid State Chem.* **1995**, *114*, 406–412.

(33) Campbell, B. J.; Stokes, H. T.; Tanner, D. E.; Hatch, D. M. ISODISPLACE: a web-based tool for exploring structural distortions. *J. Appl. Crystallogr.* **2006**, *39*, 607–614.

(34) Rodríguez-Carvajal, J. Recent advances in magnetic structure determination by neutron powder diffraction. *Phys. B* **1993**, *192*, 55–69.

(35) Miller, S. C.; Love, W. F. *Tables of Irreducible Representations of Space Groups and Co-Representations of Magnetic Space Groups*; Pruett Press: Boulder, CO, 1967.

(36) Cracknell, A. P.; Davies, B. L.; Miller, S. C.; Love, W. F. *Kronecker Product Tables, Vol. 1, General Introduction and Tables of Irreducible Representations of Space Groups*; IFI/Plenum: New York, 1979.

(37) Litvin, D. B., Ed. *Magnetic Group Tables*; International Union of Crystallography: Chester, U.K., 2013.

(38) Yamaguchi, H.; Miyagai, H.; Yoshida, M.; Takigawa, M.; Iwase, K.; Ono, T.; Kase, N.; Araki, K.; Kittaka, S.; Sakakibara, T.; Shimokawa, T.; Okubo, T.; Okunishi, K.; Matsuo, A.; Hosokoshi, Y. Field-induced incommensurate phase in the strong-rung spin ladder with ferromagnetic legs. *Phys. Rev. B: Condens. Matter Mater. Phys.* **2014**, *89*, 220402.

(39) Hsieh, D.; Qian, D.; Berger, R. F.; Cava, R. J.; Lynn, J. W.; Huang, Q.; Hasan, M. Z. Unconventional spin order in the triangular lattice system NaCrO_2 : A neutron scattering study. *Phys. B* **2008**, *403*, 1341–1343.

(40) Fang, C.; Hu, J. An effective model of magnetoelectricity in multiferroics RMn_2O_5 . *Europhys. Lett.* **2008**, *82*, 57005.

(41) Keller, L.; Dönnl, A.; Kitazawa, H.; van den Brandt, B. Geometrical frustration and incommensurate magnetic ordering in CePdAl : a low-temperature neutron-diffraction study. *Appl. Phys. A: Mater. Sci. Process.* **2002**, *74*, s686–s688.

(42) Zhao, L. L.; Wu, S.; Wang, J. K.; Hodges, J. P.; Broholm, C.; Morosan, E. Quasi-two-dimensional noncollinear magnetism in the Mott insulator $\text{Sr}_2\text{Fe}_2\text{OS}_2$. *Phys. Rev. B: Condens. Matter Mater. Phys.* **2013**, *87*, 020406.

(43) Dyar, M. D.; Agresti, D. G.; Schaefer, M. W.; Grant, C. A.; Sklute, E. C. Mössbauer Spectroscopy of Earth and Planetary Materials. *Annu. Rev. Earth Planet. Sci.* **2006**, *34*, 83–125.